Detection and characterization of singly deuterated silylene, SiHD, via optical spectroscopy

Damian L. Kokkin, Tongmei Ma, Timothy Steimle, and Trevor J. Sears

Citation: The Journal of Chemical Physics **144**, 244304 (2016); doi: 10.1063/1.4954702
View online: http://dx.doi.org/10.1063/1.4954702
View Table of Contents: http://aip.scitation.org/toc/jcp/144/24
Published by the American Institute of Physics

Detection and characterization of singly deuterated silylene, SiHD, via optical spectroscopy

Damian L. Kokkin,[1] Tongmei Ma,[1] Timothy Steimle,[1,a)] and Trevor J. Sears[2]
[1]*School of Molecular Sciences, Arizona State University, Tempe, Arizona 85287-1604, USA*
[2]*Department of Chemistry, Brookhaven National Laboratory, Upton, New York 11973-5000, USA and Chemistry Department, Stony Brook University, Stony Brook, New York 11794, USA*

(Received 25 April 2016; accepted 13 June 2016; published online 27 June 2016)

Singly deuterated silylene has been detected and characterized in the gas-phase using high-resolution, two-dimensional, optical spectroscopy. Rotationally resolved lines in the $0_0^0\tilde{X}^1A' \rightarrow \tilde{A}^1A''$ band are assigned to both *c*-type perpendicular transition and additional parallel, axis-switching induced bands. The extracted rotational constants were combined with those for SiH_2 and SiD_2 to determine an improved equilibrium bond length, r_{SiH}, and bond angle, θ, of 1.5137 ± 0.0003 Å and 92.04° ± 0.05°, and 1.4853 ± 0.0005 Å and 122.48° ± 0.08° for the $\tilde{X}^1A'(0,0,0)$ and $\tilde{A}^1A''(0,0,0)$ state respectively. The dispersed fluorescence consists of a long progression in the $\tilde{A}^1A''(0,0,0) \rightarrow \tilde{X}^1A'(0,\nu_2,0)$ emission which was analyzed to produce vibrational parameters. A strong quantum level dependence of the rotationally resolved radiative decay curves is analyzed. *Published by AIP Publishing.* [http://dx.doi.org/10.1063/1.4954702]

I. INTRODUCTION

Understanding the observed electronic state energy ordering for silylene, SiH_2, which is $\tilde{X}^1A_1 < \tilde{a}^3B_1 < \tilde{A}^1B_1 < \tilde{B}^1A_1$, relative to the energy ordering for methylene, CH_2, which is $\tilde{X}^3B_1 < \tilde{a}^1A_1 < \tilde{b}^1B_1 < \tilde{c}^1A_1$, has been of long standing theoretical interest, as has understanding the associated excited state unimolecular dynamics. Modelling the role of SiH_2 in the fabrication of amorphous silicon thin films and polycrystalline silicon has also attracted significant interest.[1–6] Motivated primarily by the desire to garner a fundamental understanding of the properties of this simplest of silicon containing polyatomic molecules, and in part by the desire to develop a real time, *in situ* SiH_2 monitoring scheme, there have been numerous reported experimental[7–28] and theoretical[29–48] studies of gas-phase SiH_2, and to a lesser extent SiD_2. In addition, SiH_2 is predicted to be abundant in circumstellar envelopes of carbon rich stars[49] and has been tentatively identified[50,51] via the detection of the 1_{11}-0_{00} pure rotational transition. In contrast to the extensive studies of the SiH_2 and SiD_2 isotopologues, the only previous experimental study of singly deuterated silylene (SiHD), which is the focus of this report, is the matrix isolated infrared spectroscopic study from which the fundamental vibrational frequencies of the $\tilde{X}^1A'$ state were determined.[52] The reduced symmetry of SiHD as compared to SiH_2 and SiD_2 causes the permanent electric dipole moment, $\vec{\mu}_{el}$, to have non-vanishing components on both the *a*- and *b*-inertial axes. Consequently, the number of electric dipole allowed, pure rotational transitions, and the number of levels that strongly Stark tune are significantly more numerous. In addition, the reduced symmetry of SiHD causes the inertial axes of the $\tilde{A}^1A''$ state to be rotated relative to that of the $\tilde{X}^1A'$ state, phenomena referred to as "axis-switching."[53–58] This leads to additional branch features in the electronic spectrum of SiHD relative to those for SiH_2 and SiD_2. This richer spectrum facilitates the extraction of structural parameters, investigation of dynamics, and provides additional possibilities for optical Stark spectroscopy.

A brief synopsis of the previous studies of SiH_2 and SiD_2 is warranted. The visible spectrum of SiH_2 was first detected in the gas-phase in 1967 by Dubois, Herzberg, and Verma[7] using conventional visible absorption spectroscopy and rotationally analyzed soon thereafter.[8] The spectrum was assigned to a progression in the ν_2'-bending mode of a *c*-type ($\Delta J = 0, \pm1$, $\Delta K_a = \pm1, \pm3 \ldots$ $\Delta K_c = 0, \pm2, \ldots$) $\tilde{X}^1A_1 \rightarrow \tilde{A}^1B_1$ electronic transition. The visible spectrum exhibits numerous local perturbations because of strong interactions amongst the $\tilde{X}^1A_1$, $\tilde{A}^1B_1$ ($E_0 \approx 1.9256$ eV[20]), $\tilde{B}^1A_1$ ($E_0 \approx 3.37$ eV[45]), and $\tilde{a}^3B_1$ ($E_0 \approx 0.9$ eV[42]) states, which correlate to the $^1\Sigma^+$, $^3\Sigma^-$, and $^1\Delta$ states arising from the $\ldots\pi^2$ configuration in a linear structure. Laser induced fluorescence (LIF) detection of the visible bands was first reported in 1980s[10,11] and at about the same time by intracavity absorption.[12] The sample was prepared by photolysis and microwave discharge under bulb conditions. The fluorescence lifetimes of $\tilde{A}^1B_1(0,\nu_2,0)$ levels of a bulb sample were measured during this period both broad banded[10] and at rotational resolution.[10,13–15] The observed lifetimes varied widely depending upon the specific rovibronic level excited, and the decay curves were often biexponential.[14] The behavior was interpreted as coupling of the $\tilde{A}^1B_1(0,\nu_2,0)$ levels with background levels in the $\tilde{X}^1A_1$ and $\tilde{a}^3B_1$ states followed by predissociation. About the same time, the adiabatic ionization potential of the $\tilde{X}^1A_1$ and $\tilde{a}^3B_1$ states of SiH_2 were experimentally determined[16] and the infrared

a)Author to whom correspondence should be addressed. Electronic mail: TSteimle@ASU.edu

diode laser absorption spectrum of the ν_2 band of the $\tilde{X}^1A_1$ state was recorded and analyzed.[17]

The first LIF detection of a supersonic free-jet expansion sample of SiH_2 and SiD_2 was performed by Fukashima *et al.*[18] Both excitation and dispersed fluorescence spectra were measured for the $(0,0,0)\tilde{X}^1A_1 \rightarrow (0,v_2,0)\tilde{A}^1B_1$, v_2 = 0-6, bands. It was proposed that the observed anomalous branch intensities were due to rotational and vibrational level-dependent nonradiative processes. The same group re-recorded the LIF excitation spectra of numerous bands of the $\tilde{X}^1A_1 \rightarrow \tilde{A}^1B_1$ electronic transition of SiD_2, which is much richer in features, at relatively high resolution (0.03 cm^{-1}).[19] The spectra were analyzed to produce a precise set of spectroscopic parameters for the $\tilde{X}^1A_1$ and $\tilde{A}^1B_1$ states. A similar LIF excitation and dispersed fluorescence study of a free-jet sample of SiH_2, but at lower spectral resolution was reported by Ishikawa and Kajimoto.[20] The developed LIF techniques were utilized for the detection of SiH_2 in a plasma similar to those used for fabrication of amorphous silicon thin films.[21–23]

The most accurate spectroscopic parameters for SiH_2 are from experiments performed nearly 20 years ago. In the case of the $\tilde{A}^1B_1$ state, they were derived from the analysis of cw-intracavity laser absorption and cw-cavity ring down spectrum of the 0_0^0 and 2_0^2 $\tilde{X}^1A_1 \rightarrow \tilde{A}^1B_1$ bands.[24,25] In those studies, rotational information up to $J = 16$, $K_a = 9$ was obtained from the analysis of Doppler limited spectra. A combined fit with the previous visible[7,8] and infrared[17] absorption measurements was performed. The $\tilde{X}^1A_1$ state parameters were derived from the analysis of infrared diode laser spectroscopic measurements.[26] More recently, the stimulated emission pumping spectrum has also been recorded and interpreted[27] to establish that the (0,3,0) $\tilde{a}^1B_1$ state lies approximately 9640 cm^{-1} above (0,0,0) $\tilde{X}^1A_1$. In addition, an optical-optical double resonance technique was used to detect the $\tilde{B}^1A_1$ states of SiH_2 and SiD_2.[28] The spectra were interpreted as quasilinear behavior in the $\tilde{B}^1A_1$ state with a very small barrier ($\cong$125 cm^{-1}) to linearity.

Now turning to the theoretical studies, there have been numerous *ab initio* predictions of the properties of SiH_2, with particular emphasis on understanding the state ordering[29–35,39–42,47] relative to that of CH_2, to gain insight into the unimolecular dynamics,[36,46,48] and aid in the interpretation of the spectra.[37,43–46] In addition to these electronic structure prediction, Duxbury *et al.*[38] reanalyzed the originally recorded $\tilde{X}^1A_1 \rightarrow \tilde{A}^1B_1$ absorption spectra of SiH_2[7,8] and rationalized the strong local perturbations and observed anomalous radiative lifetimes[14,15] using a semi-quantitative model. That model simultaneously accounted for the combined effects of Renner-Teller coupling of the $\tilde{X}^1A_1$ and $\tilde{A}^1B_1$ states, direct spin-orbit coupling of the $\tilde{a}^3B_1$ and $\tilde{X}^1A_1$ states, and second order spin-orbit coupling of the $\tilde{a}^3B_1$ and $\tilde{A}^1B_1$ states. A more quantitative, theoretical-based analysis of the interacting $\tilde{X}^1A_1$ and $\tilde{A}^1B_1$ states of SiH_2 and SiD_2 was carried out by Yurchenko *et al.*[43] In that study, *ab initio* calculations of the potential energy surfaces (PESs), the electric dipole moments, and the electric dipole transition moment surfaces for the $\tilde{X}^1A_1$ and $\tilde{A}^1B_1$ were performed. The PESs were used to calculate the rovibronic energies which were compared with experimental values and subsequently the PESs were modified to improve the agreement. Using these refined PESs for the $\tilde{X}^1A_1$ and $\tilde{A}^1B_1$ states, and accounting for the Renner-Teller coupling of these two states, the $\tilde{A}^1B_1 \rightarrow \tilde{X}^1A_1$ emission spectrum was simulated. The agreement between the observed and calculated spectra was relatively poor, suggesting that accounting only for the Renner-Teller coupling and not spin-orbit interaction is insufficient. The same group used a similar approach to refine a predicted PES for the $\tilde{B}^1A_1$ state for SiH_2 and SiD_2.[44] The optimized PESs were used to calculate the $\tilde{B}^1A_1$ term values and predict the rotation-vibration spectrum associated with the $\tilde{B}^1A_1$ state.

At about the same time, in an attempt to understand the $\tilde{X}^1A_1 \rightarrow \tilde{A}^1B_1 \rightarrow \tilde{B}^1A_1$ photoexcitation, the vibrational energies for the $\tilde{X}^1A_1$, $\tilde{A}^1B_1$, and $\tilde{B}^1A_1$ states of SiH_2 and SiD_2 were calculated, based on generated global PESs.[45] The vibrational levels, Franck-Condon factors (FCFs), and related transition probabilities were calculated. Renner-Teller effects were ignored. In a subsequent paper,[46] the same group investigated excited-state dynamics and the vibrational state dependence of the dissociations following the $\tilde{A}^1B_1 \rightarrow \tilde{B}^1A_1$ photoexcitation using three dimensional wave packet propagation methods. As part of that study, the vibronic energies for the $\tilde{X}^1A'$, $\tilde{A}^1A''$, and $\tilde{B}^1A'$ states of SiHD were also calculated. Interestingly, the photon energy dependence of the total photodissociation cross section was predicted to be fairly similar for SiH_2 and SiD_2, but very different from that predicted for SiHD. This marked difference in the photodissociation cross section was attributed to subtle difference in PESs for the $\tilde{A}$ and $\tilde{B}$ states and differences in vibrational wavefunctions. This is presumably associated with the fact that SiHD has C_S-symmetry compared to the C_{2v}-symmetry of SiH_2 and SiD_2.

Recently SiH_2 was selected as a venue for evaluation of the performance of time independent nonadiabatic transition state theory (NA-TST) relative to that of the more computationally demanding, quantum-based surface hopping method in an attempt to model spin-orbit induced intersystem crossing dynamics.[48] The $\tilde{X}^1A_1/\tilde{a}^3B_1$ system of SiH_2 was viewed as better suited for model studies of nonadiabatic dynamics of states involving different multiplicities than the $\tilde{X}^3B_1/\tilde{a}^1A_1$ system of CH_2, due to the larger spin-orbit coupling. The NA-TST and surface hopping methods predicted grossly different values for the $\tilde{X}^1A_1/\tilde{a}^3B_1$ intersystem crossing rates of SiH_2. There is no experimental information for the $\tilde{X}^1A_1/\tilde{a}^3B_1$ intersystem crossing, limiting assessment of the two methods employed. The effects of lowering the symmetry to that of SiHD were not considered, but should be large.

Here we report on the first LIF spectroscopic measurements of SiHD. Excitation and dispersed fluorescence spectroscopy and fluorescence decay curve measurements of the $0_0^0\tilde{X}^1A' \rightarrow \tilde{A}^1A''$ band near 643 nm have been performed. The $0_0^0\tilde{X}^1A' \rightarrow \tilde{A}^1A''$ band was selected instead of the more intense $2_0^2\tilde{X}^1A' \rightarrow \tilde{A}^1A''$ band near 580 nm in the anticipation of fewer local perturbations resulting in a richer spectrum due to a lower predissociation rate.

II. EXPERIMENTAL

Singly deuterated silylene (SiHD) was generated via a supersonic, pulsed, d.c. discharge through a mixture of silane (SiH_4) (~2%), deuterium (D_2) (~5%), and argon (~93%) at a backing pressure of approximately 400 PSI and operated at 20 Hz. The supersonic d.c. discharge source has been previously described.[59] The free-jet expansion was probed approximately 10 cm downstream. Four types of experiments were performed: (a) two dimensional (2D), medium resolution, excitation spectroscopy of the $0_0^0\tilde{X}^1A' \rightarrow \tilde{A}^1A''$ band of SiHD, and corresponding bands of SiH_2 and SiD_2 using a Nd:YAG pumped pulsed dye laser; (b) two dimensional (2D), high resolution, excitation spectroscopy of the $0_0^0\tilde{X}^1A' \rightarrow \tilde{A}^1A''$ band of SiHD using a single frequency cw-dye laser; (c) dispersed fluorescence (DF) resulting from the $0_0^0\tilde{X}^1A' \rightarrow \tilde{A}^1A''$ excitation; and (d) rovibronic resolved fluorescent lifetime measurements. The two dimensional (2D) method[60,61] used to record the excitation spectra was previously described.[62] Briefly, a 75 nm wide spectral window in the dispersed fluorescence is simultaneously monitored using a cooled, gated, intensified CCD detector attached to a 2/3 m monochromator. The CCD detector gate for the pulsed dye laser 2D spectral measurements was typically set to a 1 μs width and delayed 20 ns from the laser. The CCD detector gate for the cw-dye laser 2D measurments was typically set to 30 μs, which approximately corresponds to the transit time of the pulsed free-jet expansion through the viewing region of the LIF collection optics. The central wavelength of the 75 nm wide monochromator spectral window was usually selected to look at the off-resonance $\tilde{A}^1A''(000) \rightarrow \tilde{X}^1A'(010)$ emission and was tracked with the wavelength of the laser excitation source. The entrance slit width of the monochromator was set to produce a spectral resolution of approximately ±2 nm for the DF. Typically, in the 2D measurements, 30 free-jet expansion pulses were averaged at a given laser excitation wavelength. A calibrated commercial wavemeter was used to determine the absolute wavenumber of the pulsed dye laser. The transition wavenumbers of the high-resolution 2D spectra were accurately determined by simultaneously measuring the sub-Doppler spectrum of iodine.[63] The pulsed or cw-dye laser 2D spectra were subsequently processed to produce excitation spectra by vertically summing of the pixels of the CCD detector along a horizontal slice (e.g., the $\tilde{A}^1A''(000) \rightarrow \tilde{X}^1A'(010)$ emission).

DF spectra having higher resolution than those associated with the 2D measurments were recorded using the software provided with the camera and pulsed dye laser excitation. In these measurements, the entrance slit on the monochromator was narrowed to produce a resulting spectral resolution of approximately ±0.7 nm. The DF signal at a given emission wavelength was obtained from vertical binning of the intensified CCD detector. Typically in this mode of operation, 10 000 averages were taken for each 75 nm monochromator transmission window. The multiple 75-nm-wide, one-dimensional arrays of intensity versus dispersed fluorescence wavelength were spliced together, and adjusted for wavelength variation of sensitivity, to produce the DF spectra. Wavelength calibration of the DF spectra was achieved by recording the emission of an argon pen lamp. The calibration lines also facilitated the splicing together of the 75-nm-wide segments.

The fluorescence decay curves were measured by tuning the laser wavelength to be resonant with a particular feature of the excitation spectra and recording the DF spectrum at variable time delays from the pulsed laser. The gate for the CCD detector was set to a large value (approximately 1 μs) and the time delay from the laser excitation stepped in 20 ns increments to produce a series of DF spectra. The

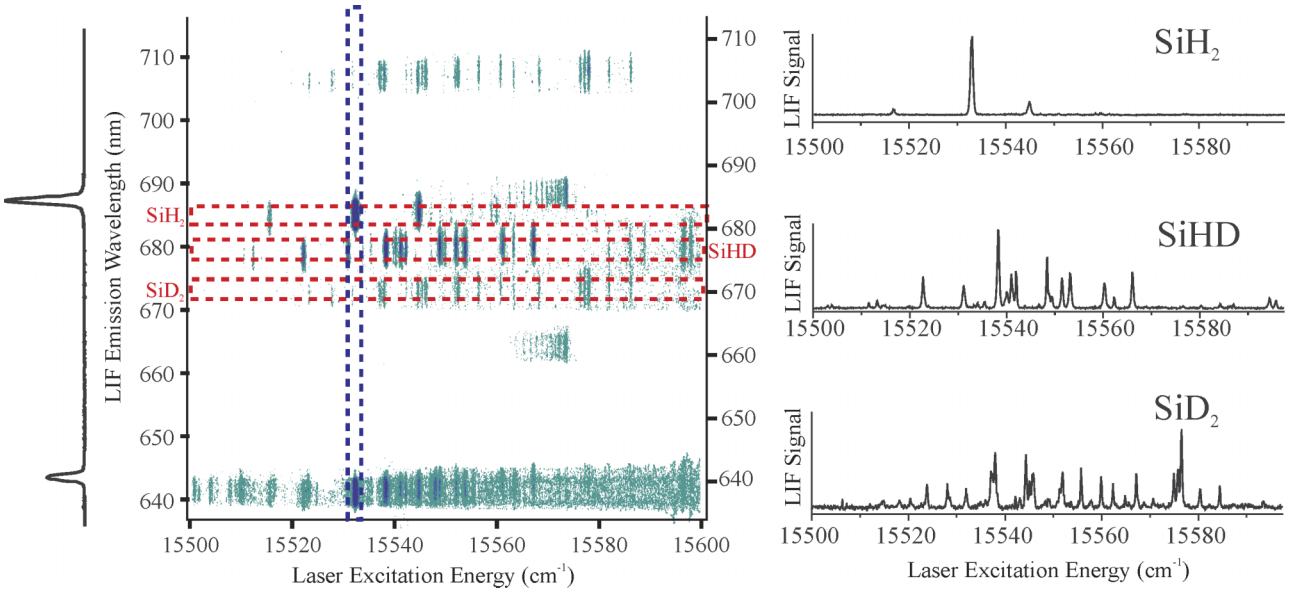

FIG. 1. Center: The pulsed dye laser, two dimensional (2D) spectrum of silylene radicals generated in a $SiH_4 + D_2$ supersonic, d.c. discharge expansion. Right: The off-resonance detected laser excitation spectra obtained from the vertical integration of the intensities of the three horizontal slices marked by the dashed red rectangles. Left: The dispersed fluorescence (DF) spectrum resulting from laser excitation of $^pP_1(1)$ $0_0^0\tilde{X}^1A_1 \rightarrow \tilde{A}^1B_1$ transition of SiH_2 at 15 532 cm^{-1}. The spectrum was obtained from the horizontal integration of the intensities of the vertical slice marked by the dashed blue rectangle.

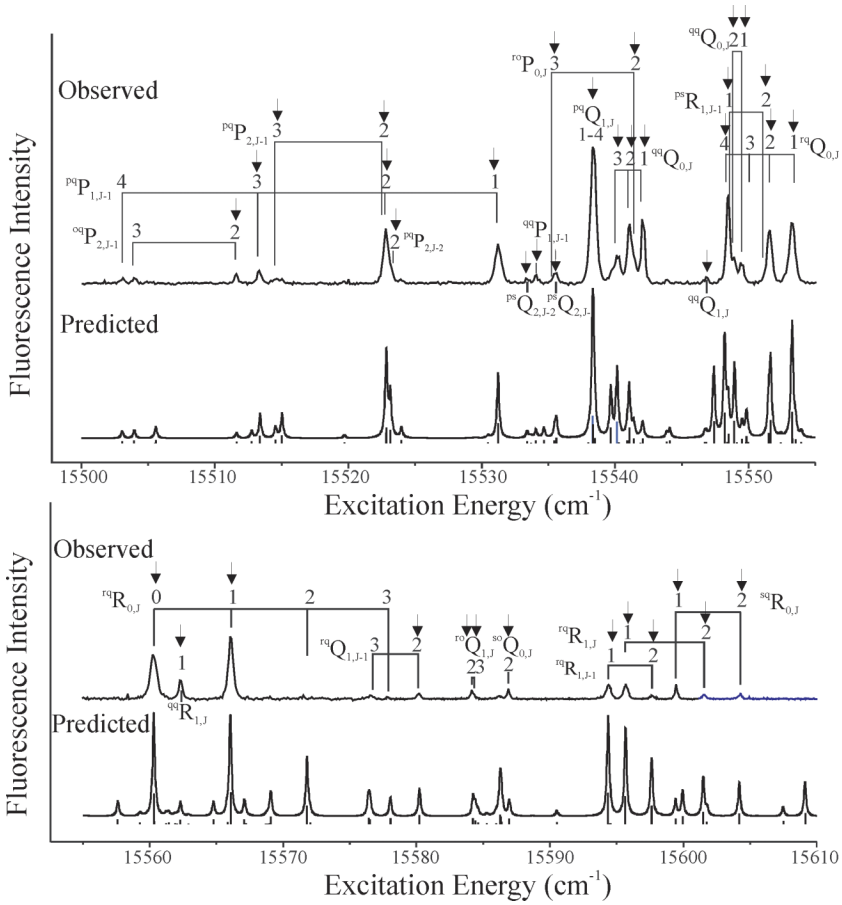

FIG. 2. The observed and predicted spectra laser excitation spectrum for the $0_0^0 \tilde{X}^1A' \rightarrow \tilde{A}^1A''$ band of SiHD and the associated assignment. The predicted stick spectrum and predicted spectrum assuming a Lorentzian line shape with a FWHM of 0.3 cm^{-1} obtained using the optimized spectroscopic parameters (*vide infra*). The features marked with arrows were recorded at high-resolution and used in the analysis.

resulting DF spectra were integrated over the appropriate wavelength region to give the relative fluorescence intensity at a given delay from the laser excitation. The lower limit of the lifetime measurements of this experimental approach is set by the approximate 20 ns pulse width of the dye laser. Typically 10^4 pulses at a given time delay were co-added resulting in a large background ($\sim 2 \times 10^6$) signal due to dark current.

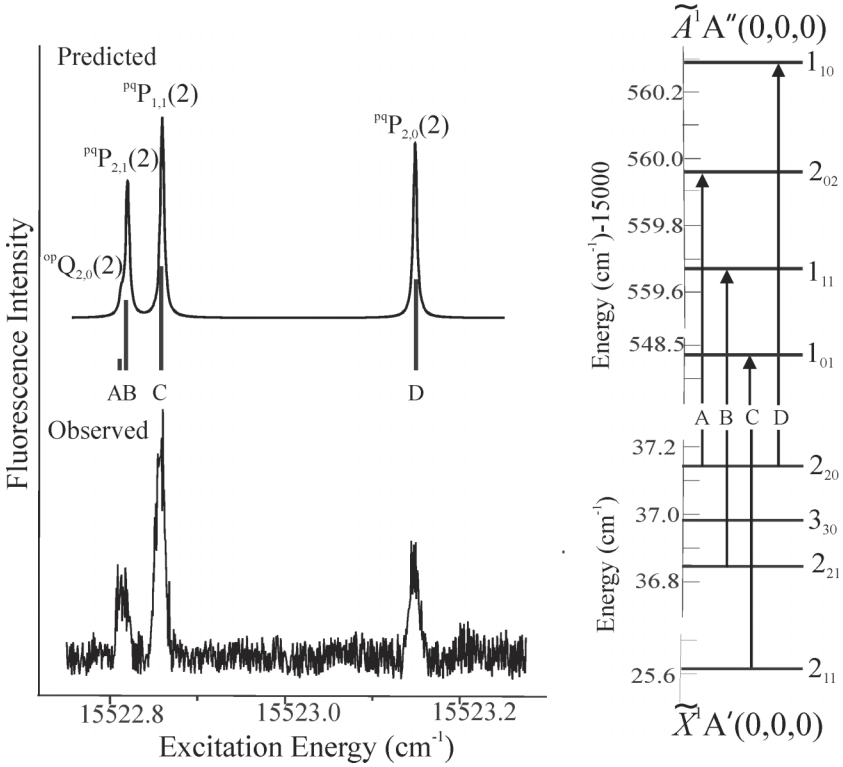

FIG. 3. Left: A 15 GHz region of the observed and predicted high-resolution LIF excitation spectrum near 15 523.0 cm^{-1}. A 200 MHz FWHM Lorentzian line was used in the prediction. Right: The associated energy levels, quantum assignment, and branch feature assignments right side of Figure 3. The three intense features are *c*-type whereas the weak, unresolved feature is an axis-switching induced transition.

TABLE I. Observed and calculated transition wavenumbers (cm^{-1}) for the $0_0^0\tilde{X}^1A' \rightarrow \tilde{A}^1A''$ band of SiHD.

Assignment		WN (cm^{-1})[a]	Obs.-Calc.	Assignment		WN (cm^{-1})[a]	Obs.-Calc.
$^{oq}P_{21}(2)$	1_{01}-2_{21}	511.6179	−0.0035	$^{pq}R_{10}(1)$	2_{02}-1_{10}	548.4776	−0.0014
$^{pq}P_{12}(3)$	2_{02}-3_{12}	513.3830	0.0013	$^{qq}Q_{12}(2)$	2_{12}-2_{12}	548.9514	0.0006
$^{pq}P_{22}(3)$	2_{12}-3_{22}	514.5400	−0.0004	$^{qq}Q_{11}(1)$	1_{11}-1_{11}	549.5202	−0.0018
$^{pq}P_{21}(2)$	1_{11}-2_{21}	522.8187	−0.0049	$^{ps}R_{11}(2)$	3_{03}-2_{11}	551.5268	0.0023
$^{pq}P_{11}(2)$	1_{01}-2_{11}	522.8616	−0.0014	$^{rq}Q_{02}(2)$	2_{12}-2_{02}	551.6623	0.0005
$^{pq}P_{20}(2)$	1_{10}-2_{20}	523.1525	0.0064	$^{rq}Q_{01}(1)$	1_{11}-1_{01}	553.2679	−0.0049
$^{pq}P_{10}(1)$	0_{00}-1_{10}	531.2283	0.0008	$^{rq}R_{00}(0)$	1_{10}-0_{00}	560.2951	0.0058
$^{ps}Q_{20}(2)$	2_{12}-2_{20}	533.4157	0.0029	$^{qq}R_{11}(1)$	2_{11}-1_{11}	562.2898	−0.0018
$^{qq}P_{11}(2)$	1_{11}-2_{11}	534.0653	0.0000	$^{rq}R_{01}(1)$	2_{11}-1_{01}	566.0411	−0.0013
$^{ro}P_{03}(3)$	2_{11}-3_{03}	535.4576	−0.0001	$^{rq}Q_{11}(2)$	2_{21}-2_{11}	580.2206	0.0024
$^{pq}Q_{21}(2)$	2_{11}-2_{21}	535.593	−0.0002	$^{ro}Q_{12}(2)$	2_{20}-2_{12}	584.2425	−0.0008
$^{pq}Q_{11}(1)$	1_{01}-1_{11}	538.3212	0.0015	$^{ro}Q_{13}(3)$	3_{21}-3_{13}	584.6116	0.0001
$^{pq}Q_{12}(2)$	2_{02}-2_{12}	538.3557	0.0010	$^{so}Q_{02}(2)$	2_{20}-2_{02}	586.9522	−0.0022
$^{pq}Q_{13}(3)$	3_{03}-3_{13}	538.5077	0.0008	$^{rq}R_{10}(1)$	2_{20}-1_{10}	594.3686	0.0010
$^{qq}Q_{03}(3)$	3_{03}-3_{03}	540.1481	0.0007	$^{rq}R_{11}(1)$	2_{21}-1_{11}	595.676	0.0011
$^{qq}Q_{02}(2)$	2_{02}-2_{02}	541.0649	−0.0009	$^{rq}R_{11}(2)$	3_{21}-2_{11}	597.6255	−0.0037
$^{ro}P_{02}(2)$	1_{10}-2_{02}	541.3986	0.0032	$^{sq}R_{01}(1)$	2_{21}-1_{01}	599.4254	−0.0004
$^{qq}Q_{01}(1)$	1_{01}-1_{01}	542.0695	−0.0011	$^{rq}R_{12}(2)$	3_{22}-2_{12}	601.4955	0.0007
$^{qq}Q_{11}(2)$	2_{11}-2_{11}	546.8315	−0.0033	$^{sq}R_{02}(2)$	3_{22}-2_{02}	604.2077	0.0019
$^{qq}Q_{13}(3)$[b]	3_{13}-3_{13}	548.2339	(0.0199)	Std. dev. Of fit = 0.0028 cm^{-1}			
$^{rq}Q_{04}(4)$	4_{14}-4_{04}	548.2530	−0.0010				

[a]Transition wavenumber (cm^{-1}) −15 000.
[b]Not included in fit.

III. OBSERVATIONS

The pulsed dye laser 2D spectrum in the 15 500 cm^{-1} to 15 600 cm^{-1} spectral region, which coincides with excitation of the $0_0^0\tilde{X}^1A' \rightarrow \tilde{A}^1A''$ band of SiHD and the $0_0^0\tilde{X}^1A_1 \rightarrow \tilde{A}^1B_1$ bands of SiH_2 and SiD_2, is presented in the center panel of Figure 1. The laser excitation wavelength is indicated on the horizontal axis and the DF wavelength on the vertical axis. Tracking the monochromator causes the vertical axis (LIF Emission Wavelength) to vary nearly linearly as function of excitation wavelength; at the beginning of the scan (15 500 cm^{-1}), the center of the 75 nm spectral window is 677.5 nm whereas at the end of the scan (15 600 cm^{-1}), it is 681.7 nm. The widely spaced features in the middle of the 2D spectra correspond to the $\tilde{A}^1A''(000) \rightarrow \tilde{X}^1A'(010)$ and $\tilde{A}^1B_1(000) \rightarrow \tilde{X}^1A_1(010)$ emissions resulting from exciting the $0_0^0\tilde{X}^1A' \rightarrow \tilde{A}^1A''$ band of SiHD and the $0_0^0\tilde{X}^1A_1 \rightarrow \tilde{A}^1B_1$ bands of SiH_2 and SiD_2, respectively. The DF near 710 nm is the $\tilde{A}^1B_1(000) \rightarrow \tilde{X}^1A_1(020)$ emission associated with the excitation of the SiH_2 $0_0^0\tilde{X}^1A_1 \rightarrow \tilde{A}^1B_1$ band. The two compact, red-degraded bands in the DF spectra near 668 nm and 692 nm are tentatively identified[64] as the (7,1) $F \rightarrow X$

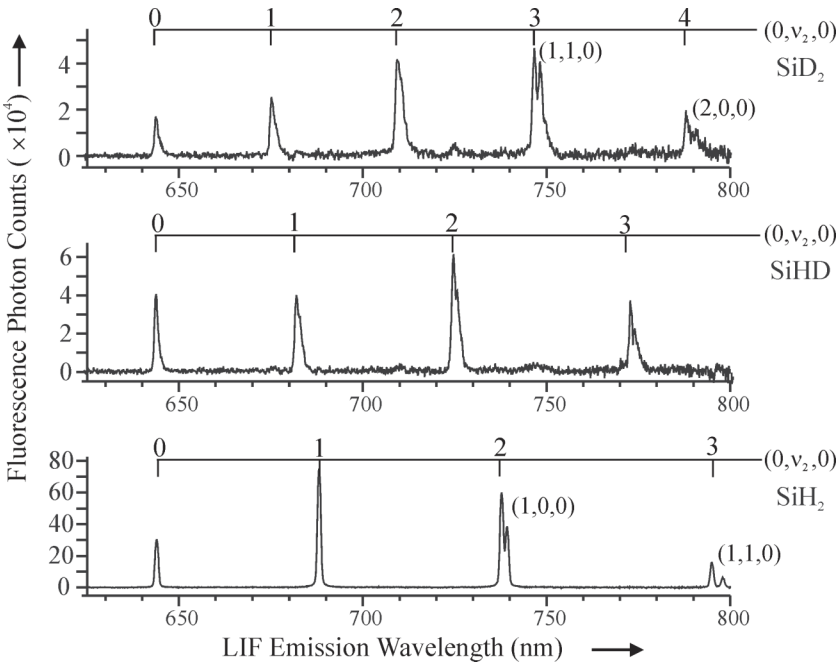

FIG. 4. The dispersed fluorescence spectra for SiH_2 (bottom), SiHD (middle), and SiD_2 (top) resulting from pulsed dye laser excitation of the $^{p}P_1(1)$ (ν = 15 532.5 cm^{-1}), $^{pq}Q_{11}(1)$ (ν = 15 538.3 cm^{-1}), and $^{p}R_1(1)$ (ν = 15 542.3 cm^{-1}) transitions, respectively.

and (7,2) $F \rightarrow X$ emissions resulting from the laser excitation of the (7,0) $F \leftarrow X$ band of Si_2 near 15 572 cm^{-1}.

At the right side of Figure 1 are the off-resonance detected laser excitation spectra obtained from the vertical integration of the intensities of the three horizontal slices marked by the dashed red rectangles. The SiH_2 (top) and SiD_2 (bottom) spectra are very similar to previously reported LIF spectra of a jet-cooled sample.[18,19] In those earlier studies, the spectral congestion was avoided by using either phenylsilane (φ-SiH_3) or phenylsilane-α-d_3 (φ-SiD_3) as a precursor in a photolysis scheme for generating either a nearly pure SiH_2 or SiD_2 sample. Here DF wavelength selectivity of the 2D spectroscopic technique is exploited to extract the spectra of the individual isotopologues from the mixed isotopologue sample. The on-resonance excitation spectrum (not shown) obtained by vertical integration of the band near 642 nm in the 2D spectrum results in an unassignable, highly overlapped spectrum of SiH_2, SiD_2, SiHD, and Si_2. The 1 μs CCD detector gate width biases against the detection of levels that pre-dissociate on a short time scale. Hence, the excitation spectrum for SiH_2 (top) is very sparse compared to that of SiD_2 (bottom) where the predissociation is less extensive. Although the excitation spectrum of SiD_2 exhibits a recognizable pattern of branches, no such pattern is obvious in the corresponding spectrum of SiHD. On the left side of Figure 1 is the DF spectrum resulting from laser excitation of $^{p}P_1(1)$ $0_0^0\tilde{X}^1A_1 \rightarrow \tilde{A}^1B_1$ transition of SiH_2 at 15 532 cm^{-1}. The spectrum was obtained from the horizontal integration of the intensities of the vertical slice marked by the dashed blue rectangle. The $\tilde{A}^1B_1(0,0,0) \rightarrow \tilde{X}^1A_1(0,1,0)$ emission feature occurs at 687.6 nm.

A more detailed pulsed dye laser excitation spectrum for SiHD is presented in Figure 2. Also presented are the predicted stick spectrum and predicted spectrum assuming a Lorentzian line shape with a FWHM of 0.1 cm^{-1} obtained using the optimized spectroscopic parameters (*vide infra*). A rotational temperature of 20 K was used based upon a comparison of the observed and predicted intensities (*vide infra*) of the lines involving the lowest rotational levels, which do not predissociate. The FWHM of the predicted spectra is approximately half the observed width in order to emphasize overlapped character. A $^{\Delta Ka}\Delta^{Kc}\Delta J_{KaKc}(J'')$ designation is being used for branch feature assignment (*vide infra*). High-resolution 2D spectra of the features marked with arrows in Figure 2 were recorded by replacing the pulsed dye laser with a single frequency, cw-dye laser. The 15 GHz region of the observed and predicted high-resolution spectrum near 15 523.0 cm^{-1} is presented on the left in Figure 3. A 200 MHz FWHM Lorentzian line was used in the simulation. The associated energy levels, quantum assignment, and branch feature assignments are given on the right side of Figure 3. The three intense features are *c*-type transitions, whereas the weak, unresolved feature is an axis-switching induced transition. The 40 measured transition frequencies and assigned quantum number assignments are given in Table I. Also given are the differences between the observed and calculated transition wavenumbers and the standard deviation of the fit.

The dispersed fluorescence spectra for SiH_2, SiHD, and SiD_2 resulting from pulsed dye laser excitation of the $^{p}P_1(1)$ ($\tilde{\nu}$ = 15 532.5 cm^{-1}),[18] $^{pq}Q_{11}(1)$ ($\tilde{\nu}$ = 15 538.3 cm^{-1}), and $^{p}R_1(1)$) ($\tilde{\nu}$ = 15 542.3 cm^{-1})[19] transitions, respectively, are presented in Figure 4. The DF spectra are primarily progressions in the $(0, \nu_2'', 0)$ mode. Due to the near resonance of multiples of ν_1, ν_2, and ν_3 vibrational frequencies for the $\tilde{X}^1A_1$ state of SiH_2, and to a lesser extent for the $\tilde{X}^1A_1$ state of SiD_2, the DF spectra of these two molecules exhibit additional features from the $1\nu_1$-$2\nu_2$ Fermi resonances as well as $2\nu_1$-$2\nu_3$ Darling-Denison resonance.[18–20,65] The weaker feature on the red side of the SiHD emissions are most likely due to the $1_{01} \rightarrow 2_{11}$ transition or caused by simultaneously pumping multiple transitions. Note that the DF spectral features for SiH_2 are sharp whereas those for SiHD, and more so for SiD_2 are broader and red-degraded. This is a consequence of the predissociation which is more prevalent in SiH_2 and the fact that the long detection gate of the CCD (1 μs) biases towards the detection of long-lived levels. The $\tilde{X}^1A'$ vibronic energies, $E(\nu_1, \nu_2, \nu_3)$, extracted from the observed spacing of the DF

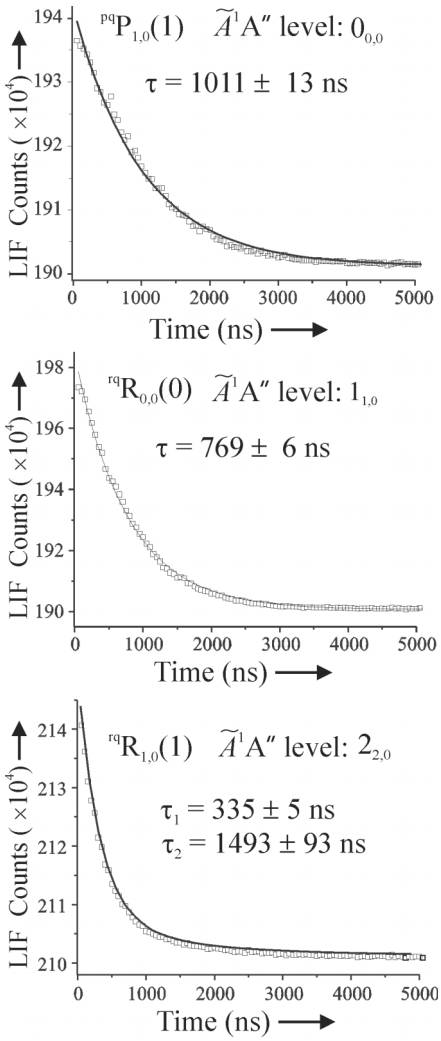

FIG. 5. The decay fluorescence curves resulting from excitation of the $^{pq}P_{10}(1)$ (ν = 15 531.2283 cm^{-1}) (top), $^{rq}R_{00}(0)$ (ν = 15 560.2951 cm^{-1}) (middle), and $^{rq}R_{10}(1)$ (ν = 15 566.0411 cm^{-1}) (bottom) transitions. The fluorescence from the $^{rq}R_{10}(1)$ line exhibits bi-exponential behavior. The amplitudes of for the bi-exponential curve are 40 016 counts (τ_1) and 5686 counts (τ_2). The associated $\tilde{A}^1A''(0,0,0)$ energy level and resulting lifetimes are indicated in Figure 8.

TABLE II. Fluorescence lifetimes (ns) and relative energies for the $A^1A''(0,0,0)$ state.

Line	Transition	Lifetime (ns)	Energy (cm^{-1})[a]
$^{pq}P_{10}(1)$	0_{00}-1_{10}	1011 ± 13	0
$^{pq}R_{10}(1)$	2_{02}-1_{10}	814 ± 4	17.25
$^{rq}R_{00}(0)$	1_{10}-0_{00}	769 ± 6	17.58
$^{rq}Q_{02}(2)$	2_{12}-2_{02}	739 ± 5	27.85
$^{rq}R_{01}(1)$	2_{11}-1_{01}	835 ± 5	29.73
$^{rq}R_{10}(1)$[b]	2_{20}-1_{10}	335 ± 5	63.14
	2_{20}-1_{10}	1493 ± 93	63.14

[a]Relative to the 0_{00} level of the $\tilde{A}^1A''$ (0,0,0) state.
[b]Bi-exponential behavior.

spectrum are E(0,1,0) = 868.3 cm^{-1}, E(0,2,0) = 1734.2 cm^{-1}, and (0,3,0) = 2589.1 cm^{-1}.

The fluorescence decay curves resulting from excitation of the $^{pq}P_{10}(1)$ ($\tilde{\nu}$ = 15 531.2283 cm^{-1}), $^{rq}R_{00}(0)$ ($\tilde{\nu}$ = 15 560.2951 cm^{-1}), and $^{rq}R_{10}(1)$ ($\tilde{\nu}$ = 15 566.0411 cm^{-1}) lines are presented in Figure 5. The decay curves associated with the $^{pq}R_{10}(1)$, $^{rq}Q_{02}(2)$, and $^{rq}R_{01}(1)$ lines were also recorded. The decay curves for all lines except the $^{rq}R_{10}(1)$ were satisfactorily fit to a single exponential function. The $^{rq}R_{10}(1)$, which has the shortest radiative lifetime, exhibited a bi-exponential behavior. The resulting lifetimes and associated errors are presented in Table II.

IV. ANALYSIS

A. Energies and transition frequencies

The SiHD DF spectrum, which exhibited a $\tilde{A}^1A''(0,0,0) \rightarrow \tilde{X}^1A'(0,\nu_2,0)$ progression, was fit to the simple anharmonic expression

$$G(0,\nu_2 0) = \omega_2(\nu_2 + 1/2) + x_{22}(\nu_2 + 1/2)^2 \quad (1)$$

to give ω_2 = 872.9(11) cm^{-1} and x_{22} = −3.2(4) cm^{-1} and a standard deviation of the fit = 2.0 cm^{-1}. The value derived from the analysis of the infrared absorption measurement of a matrix isolation sample[52] is 854.3 cm^{-1}.

Initial assignment of the *c*-type transitions in the excitation spectrum was readily accomplished by predicting the spectrum using estimated rotational parameters based upon the previously determined structure[25] of SiH_2. Combination/differences revealed that the energies were not severely perturbed. Once the assignment of the additional axis-switching transitions was obtained (*vide infra*), a direct fit to the precisely measured transition wavenumbers of Table I was performed using a non-linear least squares fitting procedure. The energies for both the $\tilde{X}^1A'$ and $\tilde{A}^1A''$ states were modelled using the standard Watson *A*-type Hamiltonian,

$$\begin{aligned}\hat{H}^{rot} = &\frac{1}{2}(B+C)\hat{J}^2 + \left[A - \frac{1}{2}(B+C)\right]J_a^2 + \frac{1}{4}(B-C)(J_+^2 + J_-^2)\\ &- \Delta_J\hat{J}^4 - \Delta_{JK}J_a^2\hat{J}^2 - \Delta_K J_a^4 - \delta_J\hat{J}^2(J_+^2 + J_-^2)\\ &- \frac{1}{2}\delta_K\left[J_a^2, (J_+^2 + J_-^2)\right]_+, \end{aligned} \quad (2)$$

where $[\,]_+$ is the anti-commutator. The eigenvalues and eigenvectors were obtained by diagonalization of a prolate symmetric top basis set representation of $\hat{H}^{rot}$. In the end, 39 of the 40 precisely measured lines were used as input to a non-linear least squares fitting procedure. In addition to the optimized rotational parameters (A_0, B_0, and C_0) and the origin (T_{00}), fits including various combinations of the centrifugal distortion parameters were attempted. Only Δ_{JK} for the $\tilde{X}^1A'$ state and Δ_K and δ_J for the $\tilde{A}^1A''$ state were required. The difference between the observed and calculated transition wavenumbers given in Table I does not exhibit any systematic pattern. The standard deviation of the fit (=0.0027 cm^{-1}) is commensurate with the estimated measurement uncertainty. The residual for the excluded $^{qq}Q_{13}(3)$ ($\tilde{\nu}$ 15 548.2339 cm^{-1}) line was 0.0186 cm^{-1}. No other transitions associated with the 3_{13} rotational level of the $\tilde{A}^1A''$ state were observed. The optimized parameters for SiHD as well as those for the previously determined values for the $\tilde{X}^1A_1$ and $\tilde{A}^1B_1$ states of SiH_2[25,26] and SiD_2[19] are given in Table III.

B. Intensities and spectral simulation

Modeling the spectrum was critical for assignment and analysis. These calculations were performed by generating

TABLE III. Spectroscopic parameters (cm^{-1}) for the $\tilde{X}^1A'(0,0,0)$ and $\tilde{A}^1A''(0,0,0)$ states of SiHD.

	SiHD[a]		SiH_2		SiD_2	
	$\tilde{X}^1A'$	$\tilde{A}^1A''$	$\tilde{X}^1A_1$[b]	$\tilde{A}^1B_1$[c]	$\tilde{X}^1A_1$[d]	$\tilde{A}^1B_1$[d]
T_{00}		15 542.709(2)		15 547.773(9)		15 539.875(2)
A_0	7.6178(17)	14.4091(23)	8.098 98(10)	18.324(2)	4.334(1)	9.6288(9)
B_0	3.8651(5)	3.1872(8)	7.023 63(8)	4.8995(9)	3.5186(5)	2.4563(7)
C_0	2.5320(4)	2.5719(8)	3.702 57(3)	3.7661(3)	1.9194(3)	1.9262(8)
Δ_J ($\times 10^{-3}$)			0.461(1)	0.089(5)	0.10(1)	0.006(7)
Δ_{JK} ($\times 10^{-3}$)	0.9(2)	17.8(5)	−1.422(5)	−0.337	−0.38(4)	−0.18(8)
Δ_K ($\times 10^{-3}$)			2.34(1)	35.2(1)	0.8(1)	8.1(3)
δ_J ($\times 10^{-3}$)		−0.52(3)	0.205 2(6)	0.041(3)	0.046(5)	0.015(3)
δ_K ($\times 10^{-3}$)					−0.037	−0.3(3)

[a]This work. The numbers in parenthesis represents a 1σ error estimate.
[b]Reference 26.
[c]Reference 25.
[d]Reference 19.

the electric dipole transition moment matrix, $\underline{\underline{\mu}}$, and then cross multiplying with the upper and lower state eigenvectors, $\underline{a}(\tilde{A}^1A'', \tilde{X}^1A')$, to obtain the appropriate transition moment, TM,

$$\mathrm{TM}(\tilde{A} \leftrightarrow \tilde{X}) = \underline{a}(\tilde{A}^1A'') \cdot \underline{\underline{\mu}} \cdot \underline{a}(\tilde{X}^1A'). \quad (3)$$

The TM was then squared and multiplied by the Boltzmann factors appropriate for the approximate 20 K internal temperature. A Lorentzian line shape was superimposed to give the predicted spectra as in Figures 1-3.

Initial simulations used the principal axis systems of the $\tilde{X}^1A'$ and $\tilde{A}^1A''$ states to calculate the eigenvectors, $\underline{a}(\text{principal})(\tilde{A}^1A'', \tilde{X}^1A')$ and transition moment matrix, $\underline{\underline{\mu}}$, to predict the relative intensities of the *c*-type transitions. The method was checked by comparing observed and predicted relative intensities for the spectral features of the $\tilde{X}^1A_1 \rightarrow \tilde{A}^1B_1$ electronic transition of SiH_2 and SiD_2. It became clear that there were many additional, non *c*-type, spectral features in the $0_0^0\tilde{X}^1A' \rightarrow \tilde{A}^1A''$ band of SiHD. Due to the C_{2v}-symmetry of SiH_2 and SiD_2, the orientation of the principal axes is unaltered upon excitation, whereas for the lower symmetry SiHD molecules, the orientation of inertial axes of the ground and excited states do not coincide. The molecule-fixed axis system is defined by the Eckart conditions, which approximately separates the rotational motion from the vibrational motion. The Eckart conditions depend upon the instantaneous geometry for the electronic state in question.[66] In order to describe an electronic transition of the molecule, two equilibrium configurations, and so two sets of moving axes must be considered. Hougen and Watson[53] showed that when a molecule undergoes an electronic transition accompanied by a geometry change, it is necessary to consider molecule-fixed axis systems of both electronic states. These axes have coincident center of mass origins, but one set is usually rotated with respect to the other. The two molecular fixed axis systems are related by a 3×3 rotation matrix **T** ("axis switching matrix").[53,55,67] The equilibria locations of the nuclei (*vide infra*) in the principal axes for the A^1A'' and $\tilde{X}^1A'$ states are shown in Figure 6. A rotation angle, Ω_0, that produces the rotation matrix, **T**, which fulfills the Eckart condition is 21.7°(Appendix). The location of the $\tilde{A}^1A''$ state nuclei in this rotated axis system (the Eckart axis system) is also shown in Figure 6, as are the angles that the principal and Eckart axes systems make relative to ones that bisect a line joining the D and H nuclei. The relative orientation of the H, D, and,

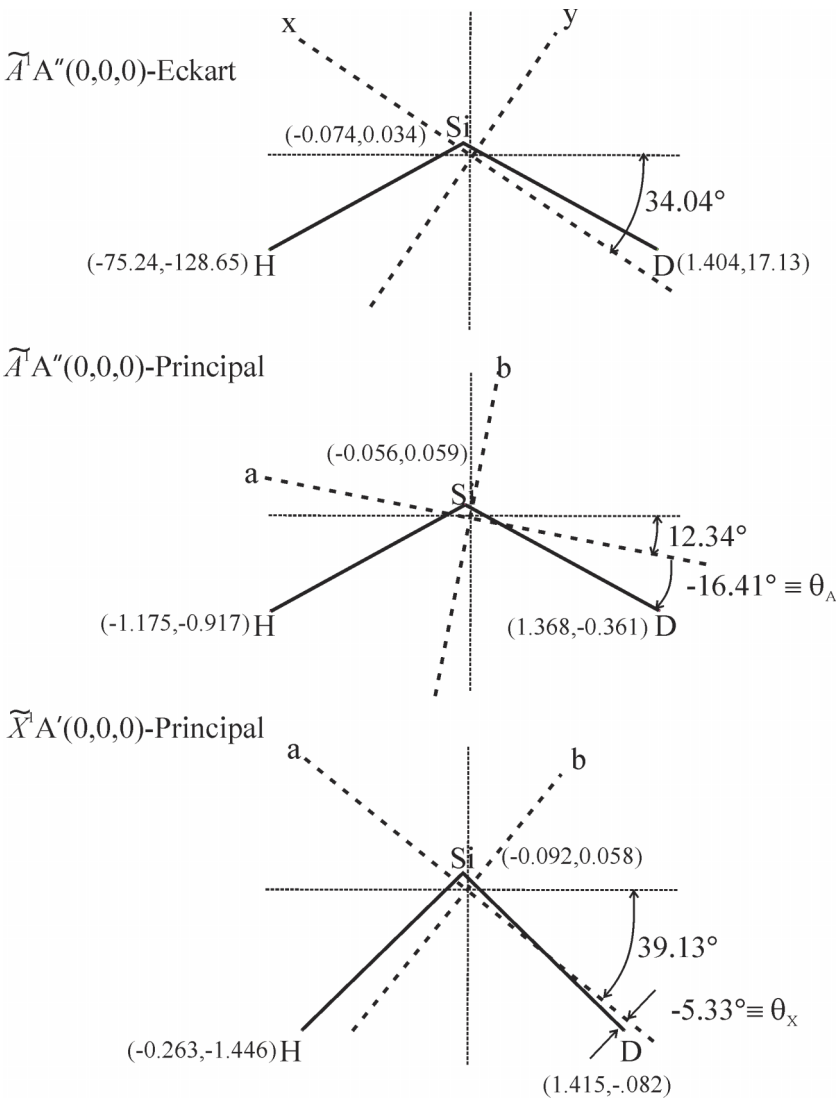

FIG. 6. The location of the nuclei in the principal axis system of the $\tilde{X}^1A'$ state (bottom), the principal axis system of the A^1A'' (middle), and the Eckart axis system of the A^1A'' state (upper). Also shown are the angles that the principle axes system make relative to one that bisects a line joining the D and H nuclei.

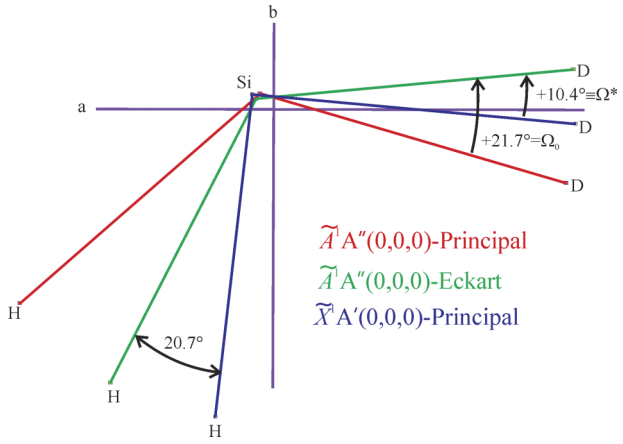

FIG. 7. The relative orientation of the H, D, and Si nuclei in the principal axis of the $\tilde{X}^1$A′ and A^1A″ states, as well as that for the A^1A″ state in an Eckart axis. Note that the 21.7° rotation of the principal axis of the A^1A″ state (see text) produces a geometry in the Eckart axis that approximately achieves a mass-weighted shift of the H and D nuclei relative to that of the $\tilde{X}^1$A′ state.

Si nuclei in the principal axes of the $\tilde{X}^1$A′ and $\tilde{A}^1$A″ states, as well as that for the A^1A″ state in the Eckart axis system, is given in Figure 7. Here the principal axes of the three are made to be coincident.

The inertial tensor in the Eckart axis system is non-diagonal and produces rotational parameters A_0, B_0, C_0, and D_0 of approximately 12.496 cm^{-1}, 4.683 cm^{-1}, 2.601 cm^{-1}, and 3.698 cm^{-1}, respectively (Appendix). These values were used to calculate the eigenvalues and eigenvectors for the $\tilde{A}^1$A″ state as described in Appendix. The Eckart axis system eigenvectors, a(Eckart)($\tilde{A}^1$A″), were then used in Eq. (3) to predict the transition moments and subsequently simulate the spectra.

V. DISCUSSION

A comparison of the observed and predicted spectra in Figure 2 reveals that numerous branch features were not observed even after accounting for the axis switching induced lines. Most obvious is the predicted $^{rq}R_{02}(2)$ transition ($3_{12} \leftarrow 2_{02}$) near 15 571.66 cm^{-1}. As other transitions originating from the 2_{02} rotational level of the $\tilde{X}^1$A′ state are observed, it was concluded that the 3_{12} rotational level of the $\tilde{A}^1$A″ state is pre-dissociative. It is also noteworthy that the 3_{13} level of $\tilde{A}^1$A″ state, which is approximately 4 cm^{-1} lower in energy than the 3_{12} level, is the upper energy terminus of the perturbed $^{qq}Q_{13}(3)$ transition (Table I). The fluorescence lifetimes of the observed branch features provide additional insight into the predissociation process. The energy level pattern with the observed lifetimes and indicated perturbed and non-observed levels is given in Figure 8. The determined lifetime of 1011 ± 13 ns for the 0_{00} level of the $\tilde{A}^1$A″ state is similar to the 1.1 ± 0.17 μs and 0.93 ± 0.38 μs values for the same rotational level of SiH_2 and SiD_2, respectively.[18] A general trend of decreasing lifetime with increasing upper state energy is observed (Table II), similar to that observed for the other isotopologues.[14,18,38] The correlation with K_a values is more pronounced with the 0_{00}, 1_{10}, and 2_{20}

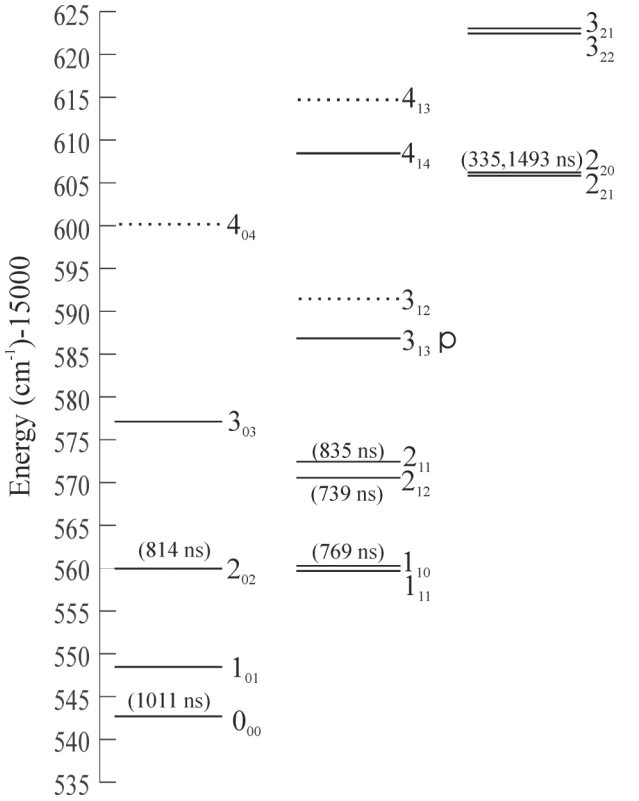

FIG. 8. The energy level pattern for the A^1A″(0, 0, 0) state of SiHD. The fluorescence lifetimes are given in parentheses. The dashed lines indicate levels that were not detected due to low fluorescence quantum yield. The 3_{13} level is slightly perturbed.

lifetimes being 1011 ns, 769 ns, and 335 ns, respectively. The 2_{11} level has a significantly longer lifetime than the 1_{10} level, which is 12 cm^{-1} lower in energy indicating that energy and/or K_a is not the only factor dictating pre-dissociation rate. The bi-exponential decay curve for the 2_{20} level is dominated by the fast component (amplitude = 40 016 counts). The lifetime of the weaker (amplitude = 5686 counts) slow component is comparable to that of the 0_{00} level. The most obvious explanation for the observed bi-exponential behavior is that two or more different transitions were simultaneously excited due to a blending of lines.[14]

The LIF excitation data set for SiHD (Table I) is less extensive than the data sets associated with the previous visible[25] or infrared[26] absorption spectra of SiH_2 due mainly to the small fluorescence quantum yield for the higher rotational levels of the $\tilde{A}^1$A″ state. Accordingly, the spectroscopic parameters for SiHD are somewhat less well determined than those for SiH_2. The precision of the determined SiHD parameters are comparable to those derived from the analysis the LIF spectrum of SiD_2,[19] but the centrifugal distortion parameters for SiD_2 are better determined because higher rotational levels were probed due to less pre-dissociation in SiD_2 compared to SiHD.

The inertial defect, Δ_0, derived from A_0, B_0, and C_0 parameters of Table III are given in Table IV. The relative small values of Δ_0 for the ground states of the three isotopologues are indicative of a rigid structure. The inertial defect is made up

of three parts, resulting from vibration and electronic motion and centrifugal distortions.[68,69] The centrifugal distortion part is usually negligible for low rotational levels. The vibrational part, $\Delta_0^{\rm vib}$, is a Coriolis effect; the electronic part, $\Delta_0^{\rm el}$, results from off diagonal matrix elements of the orbital angular momentum operator. The expression for $\Delta_0^{\rm vib}$ for molecules having C_{2V}-symmetry (e.g., SiH_2 and SiD_2) is well documented.[69] The expression for C_s-symmetry molecule (e.g., SiHD) is readily obtained from the general expression[68] and symmetry constraints[70] to be

$$\Delta_0^{\rm vib} = \frac{h}{\pi^2 c}\Bigg[\left(V_1+\frac{1}{2}\right)\left(\frac{\omega_3^2}{\omega_1(\omega_3^2-\omega_1^2)}(\zeta_{13}^{(c)})^2+\frac{\omega_2^2}{\omega_1(\omega_2^2-\omega_1^2)}(\zeta_{12}^{(c)})^2\right)$$
$$+\left(V_2+\frac{1}{2}\right)\left(\frac{\omega_3^2}{\omega_2(\omega_3^2-\omega_2^2)}(\zeta_{23}^{(c)})^2+\frac{\omega_1^2}{\omega_3(\omega_1^2-\omega_2^2)}(\zeta_{12}^{(c)})^2\right)$$
$$+\left(V_3+\frac{1}{2}\right)\left(\frac{\omega_2^2}{\omega_3(\omega_2^2-\omega_3^2)}(\zeta_{23}^{(c)})^2+\frac{\omega_1^2}{\omega_3(\omega_1^2-\omega_2^2)}(\zeta_{13}^{(c)})^2\Bigg]\Bigg). \quad (4)$$

In Eq. (4), $\zeta_{ij}^{(c)}$ are the c-principal axis component of Coriolis coupling constants between the "i-th" and "j-th" vibrational mode and ω_i is the harmonic frequency of the "i-th" mode. Theoretical predictions for $\zeta_{ij}^{(c)}$ are only available for the ground states SiH_2, SiD_2, and SiHD.[37] As part of the present study, density functional theory[71](DFT) and time dependent density functional theory[72] (TDDFT) employing the B3LYP hybrid functional[73] and the 6-311G++(3df, 3pd) basis set were used to predict $\zeta_{ij}^{(c)}$, ω_i, and vibration-rotation parameters, α_i, needed for equilibrium structure determination(*vide infra*). The DFT-B3LYP and TDDFT-B3LYP calculations were implemented using the GAUSSIAN 03 quantum chemistry program package.[74] It is not the objective to produce the best set of predicted values, but instead reasonably accurate values obtained at nearly the same level of theory for both the ground and excited states. The results are presented in supplementary material.[75] The predicted $\zeta_{ij}^{(c)}$ and ω_i values were input into Eq. (4) to predict the $\Delta_0^{\rm vib}$ values for the ground and excited states of SiHD, SiD_2 and SiH_2, and are given in Table IV. The predicted $\Delta_0^{\rm vib}$ values for the ground states of the three isotopologues are in excellent agreement with the observed Δ_0 values. In contrast, the predicted $\Delta_0^{\rm vib}$ values for the excited states are in relatively poor agreement with the observed Δ_0 values. It is reasonable that the electronic contribution to Δ_0 will be large for the excited states because of the proximity of the $\tilde{a}^3B_1$,$\tilde{A}^1B_1$, and $\tilde{B}^1A_1$ states in the case of SiH_2 and SiD_2 and the $\tilde{A}^1A''$, $\tilde{a}^3A'$, and $\tilde{B}^1A'$ states in the case of SiHD. Local perturbations in the excited state could also affect the interpretation of the rotational parameters.

The A_0, B_0, and C_0 rotational parameters of SiHD, SiH_2, and SiD_2 (Table III) were used to determine the equilibrium rotational constants, A_e, B_e, and C_e for the ground and excited states of the three isotopologues. The required

TABLE IV. Inertial defect (amu-Å^2).

Molecule	$\Delta_0(\tilde{X})$[a]	$\Delta_0^{\rm vib}(\tilde{X})$[b]	$\Delta_0(\tilde{A})$	$\Delta_0^{\rm vib}(\tilde{A})$[b]
SiHD	0.083 4(2)	0.0884	0.095 4(2)	0.1035
SiH_2	0.072 75(3)	0.0771	0.115 49(4)	0.0897
SiD_2	0.102 29(7)	0.1071	0.137 75(6)	0.1243

[a]The numbers in parenthesis represents a 1σ error estimate.
[b]Calculated using Eq. (4) and the DFT predicted Coriolis constants and vibrational frequencies (supplementary material).

TABLE V. Equilibrium rotational parameters.

	$\tilde{X}^1A'$ or $\tilde{X}^1A_1$								
	SiH_2			SiHD			SiD_2		
α[a]	0.005 81	0.040 36	0.140 02	−0.057 97	0.021 79	0.077 21	0.002 46	0.014 37	0.051 82
$v=0$[b]	8.098 98	7.023 63	3.702 57	7.617 67	3.864 95	2.531 93	4.334 50	3.518 56	1.919 45
Equal.[c]	8.101 88	7.043 81	3.772 58	7.588 69	3.875 85	2.570 54	4.335 73	3.525 75	1.945 36
	$\tilde{A}^1A''$ or $\tilde{A}^1B_1$								
	SiH_2			SiHD			SiD_2		
α[a]	−1.495 40	0.057 05	0.151 87	−1.011 03	0.041 75	0.084 70	−0.561 98	0.020 13	0.056 59
$v=0$[b]	18.324 10	4.899 51	3.766 11	14.409 08	3.187 13	2.571 86	9.628 78	2.456 23	1.926 21
Equal.[c]	17.576 40	4.928 04	3.842 05	13.903 57	3.208 01	2.614 21	9.347 79	2.466 30	1.954 51

[a]The predicted rotation-vibration parameters (see text).
[b]The experimentally determined A_0, B_0, and C_0 values from Table III.
[c]The equilibrium rotational parameters A_e, B_e, and C_e.

TABLE VI. Geometrical structure.

	$\tilde{X}^1A'$ or $\tilde{X}^1A_1$		$\tilde{A}^1A''$ or $\tilde{A}^1B_1$	
	r_e (Å)[a]	θ_e (deg)	r_e (Å)	θ_e (deg)
SiHD	1.5145(8)	91.2(6)	1.4846(11)	122.49(22)
SiH_2	1.5143(4)	92.01(4)	1.4866(6)	122.48(18)
SiD_2	1.5134(3)	92.07(2)	1.4855(6)	122.48(10)
All(SiH_2)[b]	1.5137(3)	92.04(5)	1.4853(5)	122.48(8)

[a]The numbers in parenthesis represents a 1σ error estimate.
[b]Obtained by simultaneously fitting the to the equilibrium rotational parameters of all three isotopologues.

rotation-vibration parameters, α_i, were obtained from the aforementioned electronic structure prediction. The resulting values are presented in Table V. The equilibrium geometrical parameters (r_e and θ_e) for the ground and excited states of SiHD, SiH_2, and SiD_2 were calculated from the determined A_e, B_e, and C_e parameters using the STRFIT program.[76] Fits for the individual isotopologues, as well as a global fit to all three isotopologues, are presented in Table VI. The determined r_e and θ_e for the $\tilde{X}^1A_1$ states are 1.5137(3) Å and 92.04(5)°, which compares to the most recent wavefunction-based prediction[45] of 1.5187 Å and 92.27°. The determined r_e and θ_e for the $\tilde{A}^1B_1$ state are 1.4853(5) Å and 122.48(8)°, which compares to the most recent wavefunction-based prediction[45] of 1.4904 Å and 122.70°. Other recent high-level multireference wavefunction calculations[42] give r_e and θ_e values for the $\tilde{X}^1A_1$ state that range from 1.5112 Å to 1.5171 Å and 92.52° to 92.84°, and for the excited $\tilde{A}^1B_1$ state that range from 1.4839 Å to 1.4890 Å and 121.68° to 122.26° depending upon the basis set employed.

VI. CONCLUSION

The LIF spectrum of the $0_0^0\tilde{X}^1A' \rightarrow \tilde{A}^1A''$ band of a cold sample of SiHD has been analyzed and combined with existing data for SiH_2 and SiD_2 to produce an experimentally determined structure. The LIF spectrum of SiHD is significantly more complex than that of either SiH_2 or SiD_2 mainly due to the presence of axis-switching induced transitions. The observed relative intensities of the axis-switching transitions have been successfully modeled. The inertial defects in the $\tilde{X}^1A_1$ states of SiH_2 and SiD_2 and the $\tilde{X}^1A'$ state of SiHD have been successfully modelled assuming a dominant vibronic contribution, whereas those for the excited state are inconsistent with such a model. Similar to SiH_2 and SiD_2, the fluorescence lifetimes rapidly decrease as a function of K_a from a nominal value of 1 μs for the 0_{00} level. The analysis of the optical spectrum of SiHD performed here will be relevant to future experimental and theoretical investigations of unimolecular dynamics. Optical Stark spectroscopic studies of SiHD based upon the observations presented here are being pursued in our laboratory. The determined ground state rotational parameters for SiHD will facilitate laboratory and radio telescope searches for the *a*-type (ΔK_a = even, ΔK_c = odd) and *b*-type (ΔK_a = odd, ΔK_c = odd) pure rotational transitions.

ACKNOWLEDGMENTS

This research has been supported by the National Science Foundation, Division of Chemistry, CHE-1265885 (ASU).

APPENDIX: RELATIVE INTENSITIES AND ECKART AXES

The objective is to predict the relative intensities when the effects of axis switching are considered. The 3 × 3 rotation matrix, **T**, associated with the $0_0^0\tilde{X}^1A' \rightarrow \tilde{A}^1A''$ transition is defined by Eckart conditions,[55]

$$\sum_\alpha m_\alpha(\mathbf{T}\cdot\mathbf{r}_\alpha^0(\tilde{X}))\times\left(\boldsymbol{\rho}_\alpha(\tilde{A})+\mathbf{r}_\alpha^0(\tilde{A})\right)=0, \tag{A1}$$

where $\mathbf{r}_\alpha^0(\tilde{X})$ and $\mathbf{r}_\alpha^0(\tilde{A})$ are the equilibrium position of the α-th nuclei having mass m_α in the $\tilde{X}^1A'$ and A^1A'' electronic state. $\boldsymbol{\rho}_\alpha(\tilde{A})$ is the Cartesian displacement vector of the α-th nuclei in the A^1A'' electronic state. For strongly bound molecules with low vibrational excitation, the displacement vectors are small. Under these circumstances, it is often possible to use the "zeroth order axis switching" method[53,55] that assumes that $\boldsymbol{\rho}_\alpha(\tilde{A})=0$, in which case $\mathbf{T}(\boldsymbol{\rho}_\alpha(\tilde{A})=0)\equiv\mathbf{T}_0$. The rotation matrix $\mathbf{T}_0$ depends upon the equilibria location of the nuclei in the principal axes for the A^1A'' and $\tilde{X}^1A'$ states, which are given in Figure 6. Under the "zeroth order axis switching" assumption, the Eckart conditions (Eq. (A1)) gives

$$\mathbf{T}_0=\begin{bmatrix}\cos\Omega_0 & \sin\Omega_0 & 0\\ -\sin\Omega_0 & \cos\Omega_0 & 0\\ 0 & 0 & 1\end{bmatrix}, \tag{A2}$$

where the rotation angle Ω_0 is defined by[55]

$$\tan\Omega_0=\frac{\sum_\alpha \mathrm{m}_\alpha\left(a_\alpha^\circ(\tilde{X})b_\alpha^\circ(\tilde{A})-b_\alpha^\circ(\tilde{X})\mathrm{a}_\alpha^\circ(\tilde{A})\right)}{\sum_\alpha \mathrm{m}_\alpha\left(a_\alpha^\circ(\tilde{X})\mathrm{a}_\alpha^\circ(\tilde{A})+\mathrm{b}_\alpha^\circ(\tilde{X})b_\alpha^\circ(\tilde{A})\right)}. \tag{A3}$$

In Eq. (A3), $a_\alpha^\circ(\tilde{X})$ is the *a*-principal axis location of the α-th nuclei in the$\tilde{X}^1A'$ electronic state and $b_\alpha^\circ(\tilde{A})$ is the *b*-principal axis location of the α-th nuclei in the A^1A'' electronic state. A rotation angle, Ω_0, of 21.7° is predicted using the *a*- principal axis and *b*-principal axis coordinates shown in Figure 6. The angles θ_A and θ_X shown in Figure 6 are of orientation of the Si–D bond relative to the *a*-principal axis for the A^1A'' and $\tilde{X}^1A'$ states, respectively. The relative orientation of the H, D, and Si nuclei in the principal axes of the $\tilde{X}^1A'$ and A^1A'' states, as well as that for the A^1A'' state in an Eckart axes, is given in Figure 7. Note that the 21.7° rotation of the principal axis of the A^1A'' state produces an orientation in the Eckart axis that approximately achieves a mass-weighted shift of the H and D nuclei relative to that of the $\tilde{X}^1A'$ state. Also note that $\Omega^* = \Omega_0 + (\theta_A - \theta_X)$, where Ω^* is the angle between the A^1A'' state structure in an Eckart axes and the $\tilde{X}^1A'$ structure in the principal axis system when the two systems are made to be coincident (see Figure 7).

The inertial tensor, **I**, for the A^1A'' state expressed in the Eckart axis system is (amu·Å),

$$\mathbf{I} = \begin{bmatrix} 1.761 & -1.390 & 0 \\ -1.390 & 4.698 & 0 \\ 0 & 0 & 6.458 \end{bmatrix}. \quad \text{(A4)}$$

Taking the inverse of **I** and multiplying by the appropriate constant gives the rotational Cartesian tensor (in cm^{-1}),

$$\underline{\underline{\mathbf{B}}} = \begin{bmatrix} 12.496 & 3.698 & 0 \\ 3.698 & 4.683 & 0 \\ 0 & 0 & 2.601 \end{bmatrix}. \quad \text{(A5)}$$

It is convenient to write the matrix elements of $\hat{H}^{rot}$ $(= \hat{J} \times \underline{\underline{B}} \times \hat{J})$ in spherical tensor form and express these elements in a type I^r convention axis system[70] (i.e., a right handed system with the a-principal axis = molecular fixed z-axis) prolate symmetric top basis set,

$$\langle J', k_a' | \hat{H}^{rot} | J, K_a \rangle = \delta_{J,J'}(-1)^{J'-k'}((2J+1)(J+1)J) \times \sum_{k=0}^{2}(-1)^k(2k+1)^{1/2} \begin{Bmatrix} 1 & k & 1 \\ J & J & J \end{Bmatrix} \times \begin{pmatrix} J & k & J \\ -k_a' & k_a'\text{-}q & k_a \end{pmatrix} T_q^k(B). \quad \text{(A6)}$$

In Eq. (A6), k_a is the projection of the rotational angular momentum on the a-principal axis system and $T_q^{k=0,1,2}(B)$ are the molecular fixed axis spherical tensor components of the rotational constant tensor $\underline{\underline{B}}$. The non-zero values of $T_q^{k=0,1,2}(B)$ are

$$T_0^0(B) = -\frac{1}{\sqrt{3}}(A+B+C), \quad \text{(A7)}$$

$$T_0^2(B) = \frac{1}{\sqrt{6}}(2A-B-C), \quad \text{(A8)}$$

$$T_{\pm 2}^2(B) = \frac{1}{2}(B-iC), \quad \text{(A9)}$$

$$T_{\pm 1}^2(B) = \mp D. \quad \text{(A10)}$$

It is evident from the 3j-symbol in Eq. (A6) that the off-diagonal term, D, produces a $\Delta k_a = \pm 1$ mixing of prolate symmetric top basis functions. As a consequence, in addition to the "perpendicular," c-type ($\Delta J = 0, \pm 1$, $\Delta K_a = \pm 1, \pm 3 \ldots \Delta K_c = 0, \pm 2, \ldots$) transitions, there are "parallel" $\Delta J = 0, \pm 1$, $\Delta K_a = 0, \pm 2$ transitions. The mixing of prolate symmetric top basis functions, and hence the intensities of the axis-switching induced transitions, is relatively large due to the relatively large value D. For example, the eigenvector for the $|1_{11}\rangle$ rotational level of the A^1A'' state in the principal axis system is

$$|1_{11}\rangle = \frac{1}{\sqrt{2}}\left[|J=1, k_a=+1\rangle - |J=1, k_a=-1\rangle\right], \quad \text{(A11)}$$

whereas in the Eckart axis system it is

$$|1_{11}\rangle = c_1|J=1, k_a=+1\rangle - c_1|J=1, k_a=-1\rangle + c_2|J=1, k_a=0\rangle, \quad \text{(A12)}$$

with $c_1 = 0.657$ and $c_2 = 0.370$.

[1] S. Cereda, F. Montalenti, M. Cogoni, D. Branduardi, M. W. Radny, P. V. Smith, and L. Miglio, Surf. Sci. **600**(19), 4445–4453 (2006).
[2] N. Reuge and B. Caussat, Chem. Vap. Deposition **17**(10-12), 305–311 (2011).
[3] P. Raghunath and M. C. Lin, J. Phys. Chem. A **117**(42), 10811–10823 (2013).
[4] T. Kuwahara, H. Ito, K. Kawaguchi, Y. Higuchi, N. Ozawa, and M. Kubo, J. Phys. Chem. C **117**(30), 15602–15614 (2013).
[5] H.-T. Chen and H.-W. Huang, J. Phys. Chem. C **118**(35), 20314–20322 (2014).
[6] S. Cereda, F. Montalenti, and L. Miglio, Surf. Sci. **601**(18), 3970–3973 (2007).
[7] I. Dubois, G. Herzberg, and R. D. Verma, J. Chem. Phys. **47**(10), 4262–4263 (1967).
[8] I. Dubois, Can. J. Phys. **46**(22), 2485–2490 (1968).
[9] I. Dubois, G. Duxbury, and R. N. Dixon, J. Chem. Soc., Faraday Trans. 2 **71**(4), 799–806 (1975).
[10] G. Inoue and M. Suzuki, Chem. Phys. Lett. **105**(6), 641–644 (1984).
[11] J. W. Thoman, Jr. and J. I. Steinfeld, Chem. Phys. Lett. **124**(1), 35–38 (1986).
[12] J. J. O'Brien and G. H. Atkinson, Chem. Phys. Lett. **130**(4), 321–329 (1986).
[13] Y. M. Engel, R. D. Levine, J. W. Thoman, Jr., J. I. Steinfeld, and R. I. McKay, J. Chem. Phys. **86**(11), 6561–6563 (1987).
[14] J. W. Thoman, Jr., J. I. Steinfeld, R. I. McKay, and A. E. W. Knight, J. Chem. Phys. **86**(11), 5909–5917 (1987).
[15] J. S. Francisco, R. Barnes, and J. W. Thoman, Jr., J. Chem. Phys. **88**(4), 2334–2341 (1988).
[16] J. Berkowitz, J. P. Greene, H. Cho, and B. Ruscic, J. Chem. Phys. **86**(3), 1235–1248 (1987).
[17] C. Yamada, H. Kanamori, E. Hirota, N. Nishiwaki, N. Itabashi, K. Kato, and T. Goto, J. Chem. Phys. **91**(8), 4582–4586 (1989).
[18] M. Fukushima, S. Mayama, and K. Obi, J. Chem. Phys. **96**(1), 44–52 (1992).
[19] M. Fukushima and K. Obi, J. Chem. Phys. **100**(9), 6221–6227 (1994).
[20] H. Ishikawa and O. Kajimoto, J. Mol. Spectrosc. **160**(1), 1–10 (1993).
[21] A. Kono, N. Koike, H. Nomura, and T. Goto, Jpn. J. Appl. Phys., Part 1 **34**(1), 307–311 (1995).
[22] N. M. Rubtsov, V. V. Azatyan, G. I. Tsvetkov, and S. M. Temchin, Mendeleev Commun. **7**(5), 187–188 (1997).
[23] A. Kono, S. Hirose, K. Kinoshita, and T. Goto, Jpn. J. Appl. Phys., Part 1 **37**(8), 4588–4589 (1998).
[24] A. Campargue, D. Romanini, and N. Sadeghi, J. Phys. D: Appl. Phys. **31**(10), 1168–1175 (1998).
[25] R. Escribano and A. Campargue, J. Chem. Phys. **108**(15), 6249–6257 (1998).
[26] E. Hirota and H. Ishikawa, J. Chem. Phys. **110**(9), 4254–4257 (1999).
[27] H. Ishikawa, Y. Muramoto, and N. Mikami, J. Mol. Spectrosc. **216**(1), 90–97 (2002).
[28] Y. Muramoto, H. Ishikawa, and N. Mikami, J. Chem. Phys. **122**(15), 154302 (2005).
[29] M. E. Colvin, R. S. Grev, H. F. Schaeffer III, and J. Bicerano, Chem. Phys. Lett. **99**(5-6), 399–405 (1983).
[30] J. E. Rice and N. C. Handy, Chem. Phys. Lett. **107**(4-5), 365–374 (1984).
[31] M. S. Gordon, Chem. Phys. Lett. **114**(4), 348–352 (1985).
[32] W. D. Allen and H. F. Schaefer III, Chem. Phys. **108**(2), 243–274 (1986).
[33] K. Balasubramanian and A. D. McLean, J. Chem. Phys. **85**(9), 5117–5119 (1986).
[34] C. W. Bauschlicher, Jr., S. R. Langhoff, and P. R. Taylor, J. Chem. Phys. **87**(1), 387–391 (1987).
[35] C. W. Bauschlicher, Jr. and P. R. Taylor, J. Chem. Phys. **86**(3), 1420–1424 (1987).
[36] S. Koseki and M. S. Gordon, J. Mol. Spectrosc. **123**(2), 392–404 (1987).
[37] W. Gabriel, P. Rosmus, K. Yamashita, K. Morokuma, and P. Palmieri, Chem. Phys. **174**(1), 45–56 (1993).
[38] G. Duxbury, A. Alijah, and R. R. Trieling, J. Chem. Phys. **98**(2), 811–825 (1993).
[39] Y. Yamaguchi, T. J. Van Huis, C. D. Sherill, and H. F. Schaefer III, Theor. Chem. Acc. **97**(1-4), 341–349 (1997).
[40] L. V. Slipchenko and A. I. Krylov, J. Chem. Phys. **117**(10), 4694–4708 (2002).
[41] Y. Apeloig, R. Pauncz, M. Karni, R. West, W. Steiner, and D. Chapman, Organometallics **22**(16), 3250–3256 (2003).
[42] A. Kalemos, T. H. Dunning, Jr., and A. Mavridis, Mol. Phys. **102**(23-24), 2597–2606 (2004).

[43]S. N. Yurchenko, P. R. Bunker, W. P. Kraemer, and P. Jensen, Can. J. Chem. **82**(6), 694–708 (2004).
[44]R. Guerout, P. R. Bunker, P. Jensen, and W. P. Kraemer, J. Chem. Phys. **123**(24), 244312 (2005).
[45]I. Tokue, K. Yamasaki, and S. Nanbu, J. Chem. Phys. **122**(14), 144307 (2005).
[46]I. Tokue, K. Yamasaki, and S. Nanbu, J. Chem. Phys. **124**(11), 114308 (2006).
[47]Y. A. Bernard, Y. Shao, and A. I. Krylov, J. Chem. Phys. **136**(20), 204103 (2012).
[48]R. R. Zaari and S. A. Varganov, J. Phys. Chem. A **119**(8), 1332–1338 (2015).
[49]D. D. S. MacKay and S. B. Charnley, Mon. Not. R. Astron. Soc. **302**(4), 793–800 (1999).
[50]B. E. Turner, Astrophys. J. **388**(1, Pt. 2), L35–L38 (1992).
[51]L. W. Avery, M. B. Bell, C. T. Cunningham, P. A. Feldman, R. H. Hayward, J. M. MacLeod, H. E. Matthews, and J. D. Wade, Astrophys. J. **426**(2, Pt. 1), 737–741 (1994).
[52]L. Fredin, R. H. Hauge, Z. H. Kafafi, and J. L. Margrave, J. Chem. Phys. **82**(8), 3542–3545 (1985).
[53]J. T. Hougen and J. K. G. Watson, Can. J. Phys. **43**(2), 298–320 (1965).
[54]J. M. Brown and D. A. Ramsay, Can. J. Phys. **53**(19), 2232–2241 (1975).
[55]I. Ozkan, J. Mol. Spectrosc. **139**(1), 147–162 (1990).
[56]D. M. Jonas, X. Yang, and A. M. Wodtke, J. Chem. Phys. **97**(4), 2284–2298 (1992).
[57]A. Lin, K. Kobayashi, H.-G. Yu, G. E. Hall, J. T. Muckerman, T. J. Sears, and A. J. Merer, J. Mol. Spectrosc. **214**(2), 216–224 (2002).
[58]P. Dupre, J. Chem. Phys. **134**(24), 244309 (2011).
[59]T. C. Steimle, F. Wang, X. Zhuang, and Z. Wang, J. Chem. Phys. **136**(11), 114309 (2012).
[60]N. J. Reilly, T. W. Schmidt, and S. H. Kable, J. Phys. Chem. A **110**(45), 12355–12359 (2006).
[61]J. R. Gascooke, U. N. Alexander, and W. D. Lawrance, J. Chem. Phys. **134**(18), 184301 (2011).
[62]D. L. Kokkin, T. C. Steimle, and D. DeMille, Phys. Rev. A: At., Mol., Opt. Phys. **90**(6-A), 062503 (2014).
[63]E. J. Salumbides, K. S. E. Eikema, W. Ubachs, U. Hollenstein, H. Knoeckel, and E. Tiemann, Mol. Phys. **104**(16-17), 2641–2652 (2006).
[64]K. S. Ojha and R. Gopal, Spectrochim. Acta, Part A **71A**(3), 1003–1006 (2008).
[65]H. Ishikawa and O. Kajimoto, J. Mol. Spectrosc. **174**(1), 270–273 (1995).
[66]P. R. Bunker and P. Jensen, *Molecular Symmetry and Spectroscopy*, 2nd ed. (NRCC, 1998).
[67]V. Szalay, J. Chem. Phys. **140**(23), 234107 (2014).
[68]T. Oka and Y. Morino, J. Mol. Spectrosc. **6**, 472–482 (1961).
[69]T. Oka and Y. Morino, J. Mol. Spectrosc. **8**, 9–21 (1962).
[70]W. Gordy and R. L. Cook, *Microwave Molecular Spectra*, Techniques of Chemistry Vol. 56 (John Wiley and Sons, 1984).
[71]C. Lee, W. Yang, and R. G. Parr, Phys. Rev. B: Condens. Matter **37**(2), 785–789 (1988).
[72]E. Runge and E. K. U. Gross, Phys. Rev. Lett. **52**(12), 997–1000 (1984).
[73]A. D. Becke, J. Chem. Phys. **98**(7), 5648–5652 (1993).
[74]M. J. Frisch, G. W. Trucks, H. B. Schlegel, G. E. Scuseria, M. A. Robb, J. R. Cheeseman, J. A. Montgomery, Jr., T. Vreven, K. N. Kudin, J. C. Burant, J. M. Millam, S. S. Iyengar, J. Tomasi, V. Barone, B. Mennucci, M. Cossi, G. Scalmani, N. Rega, G. A. Petersson, H. Nakatsuji, M. Hada, M. Ehara, K. Toyota, R. Fukuda, J. Hasegawa, M. Ishida, T. Nakajima, Y. Honda, O. Kitao, H. Nakai, M. Klene, X. Li, J. E. Knox, H. P. Hratchian, J. B. Cross, V. Bakken, C. Adamo, J. Jaramillo, R. Gomperts, R. E. Stratmann, O. Yazyev, A. J. Austin, R. Cammi, C. Pomelli, J. W. Ochterski, P. Y. Ayala, K. Morokuma, G. A. Voth, P. Salvador, J. J. Dannenberg, V. G. Zakrzewski, S. Dapprich, A. D. Daniels, M. C. Strain, O. Farkas, D. K. Malick, A. D. Rabuck, K. Raghavachari, J. B. Foresman, J. V. Ortiz, Q. Cui, A. G. Baboul, S. Clifford, J. Cioslowski, B. B. Stefanov, G. Liu, A. Liashenko, P. Piskorz, I. Komaromi, R. L. Martin, D. J. Fox, T. Keith, M. A. Al-Laham, C. Y. Peng, A. Nanayakkara, M. Challacombe, P. M. W. Gill, B. Johnson, W. Chen, M. W. Wong, C. Gonzalez, and J. A. Pople, GAUSSIAN 03, Revision C.02 (Gaussian, Inc., Wallingford, CT, 2004).
[75]See supplementary material at http://dx.doi.org/10.1063/1.4954702 for tables of: (a) the calculated ground state vibration rotation parameters, experimental and equilibrium rotational constants; (b) calculated excited state vibration rotation parameters, experimental and equilibrium rotational constants, and (c) calculated harmonic frequencies (cm^{-1}) and Coriolis constants.
[76]Z. Kisiel, J. Mol. Spectrosc. **218**(1), 58–67 (2003).